



Mid-Pliocene climate forcing, sea-surface temperature patterns, and implications for modern-day climate sensitivity

Michelle Dvorak,^a Kyle C. Armour,^a Ran Feng,^b Vincent T. Cooper,^a Jiang Zhu,^c Natalie Burls,^d and Cristian Proistosescu^e

^a University of Washington, Seattle, WA

^b University of Connecticut, Storrs, Connecticut

^c NSF National Center for Atmospheric Research, Boulder, Colorado

^d George Mason University, Fairfax, Virginia

^e University of Illinois Urbana-Champaign, Champaign, Illinois

Corresponding author: Michelle Dvorak, mtdvorak@uw.edu

Early Online Release: This preliminary version has been accepted for publication in *Journal of Climate*, may be fully cited, and has been assigned DOI 10.1175/JCLI-D-24-0410.1. The final typeset copyedited article will replace the EOR at the above DOI when it is published.

© 2025 American Meteorological Society. This is an Author Accepted Manuscript distributed under the terms of the default AMS reuse license. For information regarding reuse and general copyright information, consult the AMS Copyright Policy (www.ametsoc.org/PUBSReuseLicenses).

ABSTRACT: Characterized by similar-to-today CO₂ levels (~400ppm) and surface temperatures approximately 3–4°C warmer than the preindustrial, the mid-Pliocene Warm Period (mPWP) has often been used as an analog for modern CO₂-driven climate change, and as a constraint on the equilibrium climate sensitivity (ECS). However, model intercomparison studies suggest that non-CO₂ boundary conditions – such as changes in ice sheets – contribute substantially to the higher global mean temperatures and strongly shape the pattern of sea-surface warming during the mPWP. Here, we employ a set of CESM2 simulations to quantify mPWP effective radiative forcings, study the role of ocean circulation changes in shaping the patterns of sea-surface temperatures, and calculate radiative feedbacks during the mPWP. We find that the non-CO₂ boundary conditions of the mPWP, enhanced by changes in ocean circulation, contributed to larger high-latitude warming and less-stabilizing feedbacks relative to those induced by CO₂ alone. Accounting for differences in feedbacks between the mPWP and the modern (greenhouse-gas driven) climate provides stronger constraints on the high-end of modern-day ECS. However, a quantification of the forcing of non-CO₂ boundary condition changes combined with the distinct radiative feedbacks that they induce suggests that Earth System Sensitivity may be higher than previously estimated.

SIGNIFICANCE STATEMENT: Climate records from past warm intervals in Earth's geologic history are frequently used to constrain modern-day equilibrium climate sensitivity. Yet, climate warmth during these periods is not solely driven by the radiative effect of CO₂, but by environmental and geographic features, such as large-scale ice sheet and vegetation changes, that are not expected to occur in the near future. Using the mid-Pliocene warm period as an example, we find that the surface patterns of warming induced by non-CO₂ paleogeographic boundary conditions lead to a more-sensitive climate state than the modern. This implies that near-term warming under CO₂ forcing may be smaller than expected, but that on geological timescales future warming may be significantly larger.

1. Introduction

The mid-Pliocene warm period (mPWP, ~3.3–3.0 Mya) – also referred to as the mid-Piacenzian (Dowsett et al. 2016) – was an interval in Earth's history characterized by similar-to-today concentrations of atmospheric CO₂ (~400ppm; Martínez-Botí et al. 2015) but with global average temperatures approximately 3–4°C warmer than the preindustrial (Sherwood et al. 2020; Forster et al. 2021; Annan et al. 2024; Tierney et al. (submitted)). The potential for anthropogenic greenhouse gas emissions to drive global warming to similar levels has contributed to the use of this period as an analog for climate change over the 21st century (Burke et al. 2018; Tierney et al. 2020; Burton et al. 2023). It has also been used as a constraint on the equilibrium climate sensitivity (ECS) – a key metric of the long-term global temperature response to CO₂ forcing (e.g., Sherwood et al. 2020; Forster et al. 2021).

However, coupled global climate model simulations from the recent Pliocene Model Intercomparison Project phase 2 (PlioMIP2; Haywood et al. 2016) suggest that a significant fraction of the surface warming during the mPWP may have been driven by paleoenvironmental boundary conditions rather than CO₂ forcing (Lunt et al. 2012; Haywood et al. 2020; Baatsen et al. 2021; Feng et al. 2020). These include topographic anomalies resulting from reduced ice sheet extent over Greenland and Antarctica (the latter resulting in an ice-free, oceanized West Antarctica) and exposure of the Bering Strait land bridge, Arctic Archipelagic and Sunda and Suhal continental shelves in Indonesia (Figure 1), along with major changes in vegetation type and extent (Haywood et al. 2016). In simulations carried out using the US National Science Foundation National Center

for Atmospheric Research's (NSF NCAR's) fully-coupled Community Earth System Model, version 2 (CESM2; Danabasoglu et al. 2020), this set of paleoenvironmental boundary conditions, with no greenhouse gas changes relative to the preindustrial, lead to globally-averaged surface warming of 2.9°C – more than half of the 5.1°C mPWP warming in the model (Feng et al. 2020).

That more than half of the warming of the mPWP was driven by boundary condition changes implies that care must be taken when using reconstructions of this period as an analog for greenhouse-gas driven near-term warming. The standard method of inferring climate sensitivity to CO_2 from these reconstructions is by treating these slow changes as forcings, rather than as feedbacks (e.g., Sherwood et al. 2020; PALEOSENS 2012). In doing so, it has been assumed that the climate's sensitivity to changes in CO_2 and boundary conditions are similar; i.e., that all forcings produce the same amount of global warming per unit forcing.

However, recent studies of the Last Glacial Maximum (LGM) have shown that more of the cooling at the LGM came from non- CO_2 forcings (specifically land ice sheet changes) than previously recognized (Zhu and Poulsen 2021) and, thus, that ECS and near-future, greenhouse-gas driven warming can be constrained to be a lower value (Cooper et al. 2024). The mechanism by which this occurs is known as the pattern effect (Armour et al. 2013; Andrews et al. 2015; Stevens et al. 2016), whereby radiative feedbacks (mainly associated with cloud responses) depend on the spatial pattern of sea-surface temperatures (SSTs) (e.g., Dong et al. 2019; Zhou et al. 2017). Because ice sheet changes occur at high latitudes, the warming or cooling they induce also primarily occurs at high latitudes, where radiative feedbacks are relatively more positive (amplifying) (Stuecker et al. 2018). This leads to a larger global temperature response than that induced by an equivalent amount of CO_2 forcing, which peaks in the tropics and is more spatially uniform (Smith et al. 2020; Bonan et al. 2018).

Does a similar SST pattern effect on radiative feedbacks need to be accounted for when constraining ECS and future warming using reconstructions of the mPWP? To answer this question, we need a quantitative understanding of the drivers of mPWP warmth, and of the radiative feedbacks induced by CO_2 and boundary condition changes in particular. Previous studies have examined the large-scale effects of these boundary conditions on the mPWP climate with fully-coupled simulations in which paleogeography, vegetation, ice sheets, and CO_2 are modified individually (Lunt et al. 2021, 2010; Chandan and Peltier 2018; Feng et al. 2017; Haywood et al. 2016; Feng et al.

2022). The global climate response to paleogeographic changes (including continental topography and ocean bathymetry) are thought to be relatively small (Feng et al. 2017), while changes in vegetation and ice sheets are thought to contribute substantially to mPWP warmth (Chandan and Peltier 2017; Weiffenbach et al. 2023). Here we build on these findings by performing CESM2 simulations that allow us to calculate the effective radiative forcing (ERF; Forster et al. 2021, 2016) associated with mPWP CO₂ and boundary conditions. With these ERFs quantified, we are then able to calculate the radiative feedbacks induced by these changes separately, and determine whether the climate's sensitivity to mPWP forcings is different from its sensitivity to CO₂ doubling alone (which defines ECS). We also perform mixed-layer (“slab”) ocean CESM2 simulations with the same set of mPWP forcings to assess the role of ocean circulation in shaping the SST patterns that give rise to radiative feedback differences. The results have direct implications for how the mPWP can be used to constrain ECS and future warming.

We use a set of models in the CESM2 family to quantify and understand the forcings and feedbacks shaping the mPWP climate, similar in spirit to the methodology used by Zhu and Poulsen (2021) for the LGM. In what follows, we describe the models used (Section 2), provide a novel estimate of mPWP ERFs (Section 3), investigate the role of ocean circulation in shaping mPWP SST patterns (Section 4), and quantify radiative feedbacks under mPWP forcings (Section 5). Finally, we discuss the implications of our results for estimates of modern-day ECS – of relevance for near-term warming – and for the Earth System Sensitivity governing warming in the distant future (Section 6).

2. Overview of models and approach

We carry out a suite of simulations using CESM2.1 in atmosphere-only, slab ocean, and fully-coupled configurations. CESM2 is a coupled atmosphere-land-ocean-sea ice global climate model with 32 vertical levels in the atmosphere and 60 vertical levels in the oceans. In all simulations, the model incorporates the Community Atmosphere Model version 6.0 (CAM6), Community Land Model version 5.0 (CLM5), Community Ice Code (CICE) version 5, and the Parallel Ocean Program (POP) version 2. All simulations are carried out with atmosphere and land models resolved at 0.9° latitude × 1.25° longitude. Fully-coupled simulations of the preindustrial control and CO₂ forcing simulations were performed with ocean and sea ice components resolved on a

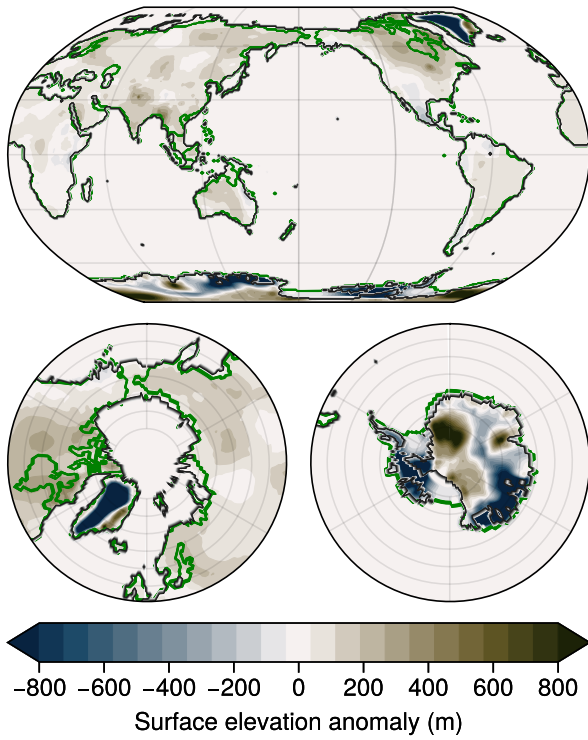


FIG. 1: PRISM4 topographic land-sea mask used as input to CESM2 mPWP simulations (Dowsett et al. 2016). Ice sheet changes are shown as surface elevation anomalies with respect to preindustrial ice sheet height. Preindustrial coastlines are shown in green while Pliocene coastlines are shown in black.

384×320 curvilinear mesh grid; mPWP simulations were performed with an expanded grid of 394×320 to resolve dynamic processes in the oceanized West Antarctica (Feng et al. 2020).

All mPWP simulations employ a set of paleoenvironmental boundary conditions developed through the most recent phase of the Pliocene Research, Interpretation and Synoptic Mapping project 4 (PRISM4) (Dowsett et al. 2016). These include global reconstructions of the land-sea mask, vegetation type and extent, soil and lake distributions, continental topography, ocean bathymetry, and ice sheet height and extent (Fig. 1). We refer to this set of features hereafter as simply “boundary conditions.” CO₂ concentrations are set to 400 ppm, while all other greenhouse gases and aerosol emissions are set to preindustrial levels, as these are not well constrained by paleoclimate reconstructions. Orbital parameters are set to those of 3.205 Ma, which is the same as the preindustrial (Haywood et al. 2016).

We make use of existing fully-coupled model (FCM) CESM2 simulations that were performed as part of the PlioMIP2 project (Feng et al. 2020; Table 1). These are: a preindustrial (PI) control simulation with CO₂ at 284.7 ppm (FCM-PI, 2000 years long); a mPWP simulation complete with mPWP-level CO₂ at 400 ppm and boundary conditions (FCM-mPWP, 1200 years long); a mPWP boundary condition-only simulation with PI-level CO₂ of 284.7 ppm (FCM-BC, 400 years long); and a simulation with PI control boundary conditions but mPWP-level CO₂ of 400 ppm (FCM-CO₂, 900 years long) (Table 1). These simulations were run with dynamical phenology while plant functional types were prescribed separately for mPWP and PI. Simulations using PI boundary conditions were initialized from the end of the 1200 year PI control simulation performed for the Coupled Model Intercomparison Project phase 6 (CMIP6; Eyring et al. 2016).

Model initialization from a warm ocean state was used to efficiently achieve quasi-equilibrium in FCM-mPWP (Feng et al. 2020). All simulations have a global top-of-atmosphere radiation imbalance of $\leq 0.25 \text{ Wm}^{-2}$ by the end of run-time (Table 1). The soil carbon reservoir (relevant for vegetation) was initialized to reach equilibrium by running standalone CLM5 with mPWP boundary conditions for 600 years (Feng et al. 2020) before carrying out the FCM-mPWP and FCM-BC simulations.

For comparison with CO₂-driven future climate change, we also make use of an existing 150-year-long simulation of CESM2, contributed to CMIP6, wherein CO₂ concentrations were abruptly doubled from PI levels (referred to here as FCM-2xCO₂). We extended this simulation for another 150 years in order to allow the model to come closer to equilibrium, permitting a more accurate estimate of the model value of ECS (e.g., Rugenstein and Armour 2021) (Section 5), which is defined by the equilibrium surface warming under CO₂ doubling.

As noted above, within these fully-coupled CESM2 simulations, boundary conditions alone account for over half of the total global mPWP surface warming (compare 2.9°C in FCM-BC to 5.1°C in FCM-mPWP – see Table 1). Meanwhile, mPWP CO₂ forcing alone accounts for less than half of mPWP warming (2.0°C in FCM-CO₂). Note that the simulated responses are relatively linear such that the sum of global temperature changes in FCM-CO₂ and FCM-BC (4.9°C) is nearly equal to the global temperature change in FCM-mPWP (5.1°C). There is substantial polar amplification of surface warming from boundary conditions when compared to CO₂ changes alone (Fig. 2 b-c). When normalized by the global mean sea-surface temperature, a pattern of

TABLE 1: Description of simulations used in this study. All values are taken as averages over the period of analysis unless otherwise noted, and anomalies are taken with respect to preindustrial control simulations.

Model set-up	Simulation long name	Simulation short name	Length (period of analysis) (years)	Global TOA radiation imbalance anomaly, ΔN (Wm^{-2})	Average global surface temperature anomaly, ΔT ($^{\circ}\text{C}$)
Fully-coupled	Preindustrial control	FCM-PI	2000 (100)	0.06	0.
	mid-Pliocene	FCM-mPWP	1200 (100)	0.25	5.10
	mid-Pliocene 284.7ppm CO ₂	FCM-BC	400 (50)	0.03	2.85
	400ppm CO ₂ only	FCM-CO ₂	900 (90)	0.14	2.01
	2xCO ₂ (569ppm)	FCM-2xCO ₂	300 (250)*	0*	4.07*
Slab ocean	mid-Pliocene	SOM-mPWP	126 (50)	0.08	4.46
	mid-Pliocene 284.7ppm CO ₂	SOM-BC	75 (50)	0.02	1.15
	400ppm CO ₂ only	SOM-CO ₂	84 (50)	-0.03	2.41
	2xCO ₂ (569ppm)	SOM-2xCO ₂	84 (50)	0.09	5.56
Atmosphere-only	mid-Pliocene	ATM-mPWP	30 (25)	3.40	0.46
	mid-Pliocene 284.7ppm CO ₂	ATM-BC	35 (30)	1.34	0.31
	400ppm CO ₂ only	ATM-CO ₂	33 (28)	2.06	0.11
	2xCO ₂ (569ppm)	ATM-2xCO ₂	33 (28)	4.27	0.26

*Period of analysis here corresponds to a regression of ΔN on ΔT over years 100-300, with the equilibrium temperature extrapolated to $\Delta N = 0 \text{ Wm}^{-2}$.

enhanced warming in the Southern Ocean, North Pacific Ocean, and North Atlantic Ocean is evident, especially in FCM-BC (Fig. 2 d-f). These warming patterns also come along with strong reductions in low cloud cover (Fig. 2 g-i), suggesting that cloud feedbacks may play a role in how mPWP boundary conditions influence global temperature.

To further probe the drivers of mPWP warmth within CESM2, we first quantify the ERF of mPWP boundary condition and CO₂ changes using atmosphere-only simulations, allowing us to determine the extent to which each contributes directly to mPWP warming. We then consider in greater detail the spatial patterns of warming induced by each forcing, and quantify the contribution of slow ocean circulation changes to surface warming patterns by comparing the existing fully-coupled model results to new slab ocean model simulations in which ocean heat transport cannot change. Finally, we use these simulations to quantify the radiative feedbacks that govern the climate's sensitivity to the different mPWP forcings and connect them to differences in warming patterns.

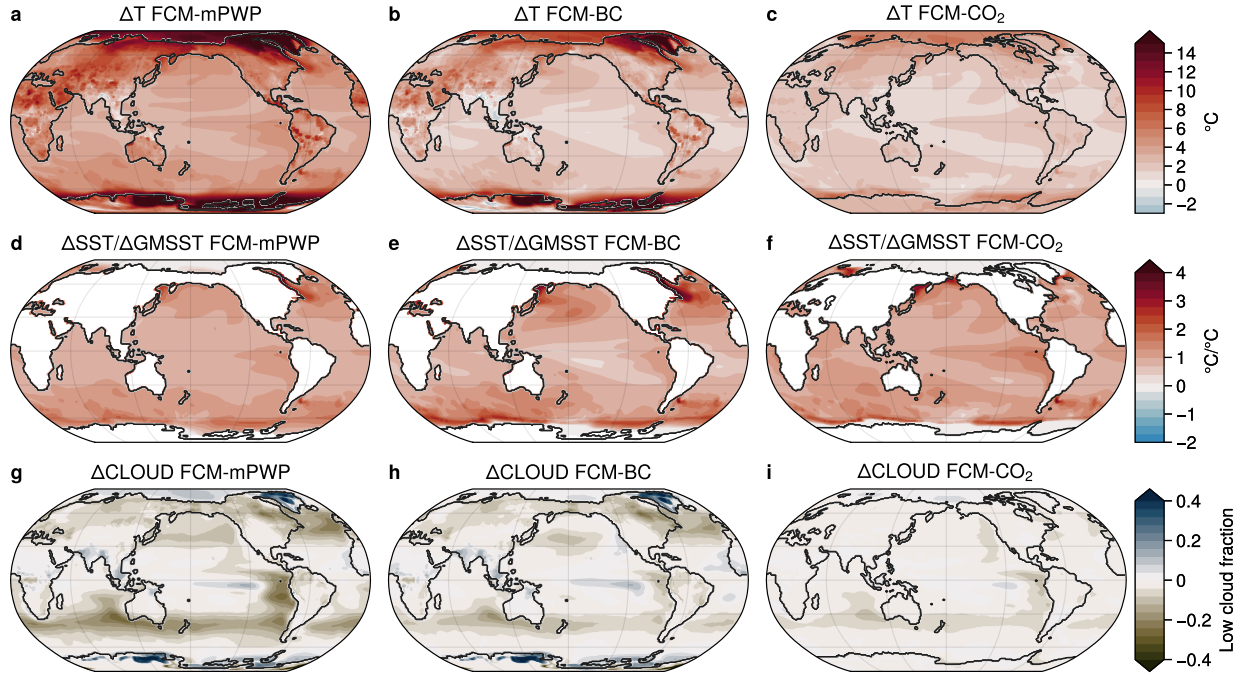


FIG. 2: Surface air temperature (a-c), sea-surface temperature normalized by global mean (d-f), and low cloud fraction (g-i) anomalies from preindustrial diagnosed from fully-coupled CESM2 simulations of mid-Pliocene forcings (FCM-mPWP), changes in boundary conditions only (FCM-BC), and changes in CO₂ only (FCM-CO₂). All panels show anomalies relative to FCM-PI.

3. mPWP effective radiative forcing (ERF)

To calculate the ERF of mPWP forcings, we follow the now-standard approach (e.g., Hansen et al. 2005; Pincus et al. 2016) of performing simulations with an atmosphere-only model (CAM6, the atmospheric component of CESM2) in which SSTs and sea ice concentrations are prescribed to match the PI climatology while boundary conditions and CO₂ forcing are imposed. We refer to these as fixed-SST simulations.

We employ a forcing-feedback framework consistent with the standard formulation of global energy balance:

$$\Delta N = \Delta F + \lambda \Delta T, \quad (1)$$

where ΔN is the global top-of-atmosphere radiation change from PI, ΔF is effective radiative forcing, ΔT is the global surface air temperature change from PI, and λ is the global radiative feedback (negative for a stable climate). Given ΔN , ERF can be estimated using equation (1) in

the case where $\Delta T \approx 0$; i.e., the average global surface temperature is unchanged with respect to the PI control. In practice, the simulations show a small amount of global mean surface warming (δT) even with fixed SSTs and sea ice concentrations. The radiative response to this warming effectively reduces ΔN and biases the ERF estimate downward. We correct for this effect by using the common Hansen et al. (2005) adjustment:

$$\Delta F = \Delta F_{fSST} - \delta T_{fSST} \lambda \quad (2)$$

where λ is the net radiative feedback estimated from the fully-coupled, abrupt CO₂-doubling simulation (FCM-2xCO₂). Note that equations (1)-(2) can also be applied to estimate shortwave (SW) and longwave (LW) components of ERF separately.

We perform five fixed-SST simulations with CAM6, denoted with ATM for atmosphere-only, corresponding to the five forcing scenarios described above for CESM2 (Table 1). We run each of these simulations for a minimum of 30 years, and exclude the first 6 years from the ERF analysis to allow for transient adjustment to the imposed forcings. In all fixed-SST simulations, sea-surface temperatures and sea ice concentration are prescribed to match values derived from the climatology of CESM2's PI control simulations. In regions of West Antarctica where the absence of grounded and floating ice shelves in the mPWP (ATM-mPWP and ATM-BC) requires the introduction of new ocean grid cells (Fig. 1), SSTs are fixed to the freezing point of seawater (-1.8°C) and sea ice concentration is set to 100%. This choice maintains a realistic ocean surface albedo in the high Southern latitudes, where SSTs are cold enough to support sea ice but no PI sea ice exists (Supplementary Fig. S1).

Using our ATM-mPWP simulation and equations (1)-(2), we calculate a total ERF of the mPWP of 3.8 Wm⁻². This accounts for changes in CO₂, land-sea mask, ice sheets, vegetation, and topography between the mPWP and the PI. This total forcing can also be quantified in terms of its SW and LW components (Table 2). We find that the ERF of mPWP boundary conditions alone (ATM-BC) is 1.7 Wm⁻², while that of CO₂ (ATM-CO₂) is 2.2 Wm⁻². Once again, the simulated responses are relatively linear such that the sum of ERFs in ATM-CO₂ and ATM-BC (3.9 Wm⁻²) is nearly equal to the ERF in ATM-mPWP (3.8 Wm⁻²).

We find significant hemispheric asymmetry in the ERF of the mPWP, with strong, positive SW forcing in the northern high latitudes due to land surface albedo changes associated with the

TABLE 2: Global average ERF and their SW and LW components.

	ΔN (Wm^{-2})	ΔF (after adjustment) (Wm^{-2})	ΔF (SW) (Wm^{-2})	ΔF (LW) (Wm^{-2})
ATM-mPWP	3.40	3.83	2.64	1.19
ATM-BC	1.34	1.65	2.28	-0.63
ATM-CO ₂	2.06	2.17	0.58	1.59
ATM-2xCO ₂	4.27	4.53	1.18	3.36

reduction of the Greenland ice sheet and increase in vegetation cover, extending from Siberia across the above-sea-level Bering Strait and North America (Fig. 3). The tropics are characterized by positive SW forcing associated with vegetation changes in sub-saharan Africa, which is slightly offset by the enhanced LW emission to space from the warmer atmosphere.

We also find slight negative SW forcing in Indonesia where the exposure of the Sunda and Sahul shelves leads to an increase in surface albedo, and negative SW forcing over the eastern tropical Pacific Ocean in ATM-mPWP and ATM-BC – possibly due to a cloud response to a change in atmospheric column temperatures and moisture favoring an increase in atmospheric stability. LW forcing is positive everywhere in ATM-CO₂ owing to higher CO₂ levels reducing outgoing LW radiation. Altogether, the total mPWP forcing is positive in most regions of the globe, except over some localized regions of the ocean, such as the eastern tropical Pacific and North Atlantic, and over Indonesia (Fig. 3).

PlioMIP studies have heretofore focused on estimating the global warming contributions of mPWP forcings through a suite of fully-coupled simulations in which boundary conditions are imposed individually (Burton et al. 2023; Baatsen et al. 2021; Lunt et al. 2012, 2010), rather than on quantifying the ERF of these individual changes. CO₂ forcing of the mPWP has been estimated using existing CO₂-driven simulations (e.g., CO₂ doubling) under the assumption that CO₂ forcing scales logarithmically with concentration (Sherwood et al. 2020; Haywood et al. 2020; Feng et al. 2020).

The explicit quantification of mPWP ERF, and its separation into contributions from boundary condition and CO₂ changes, presented here, is the first to use fixed-SST simulations, which are necessary for accurate ERF estimation (e.g., Andrews et al. 2021; Zhu and Poulsen 2021). This approach is consistent with the CMIP6 protocol for estimating ERF (Smith et al. 2020).

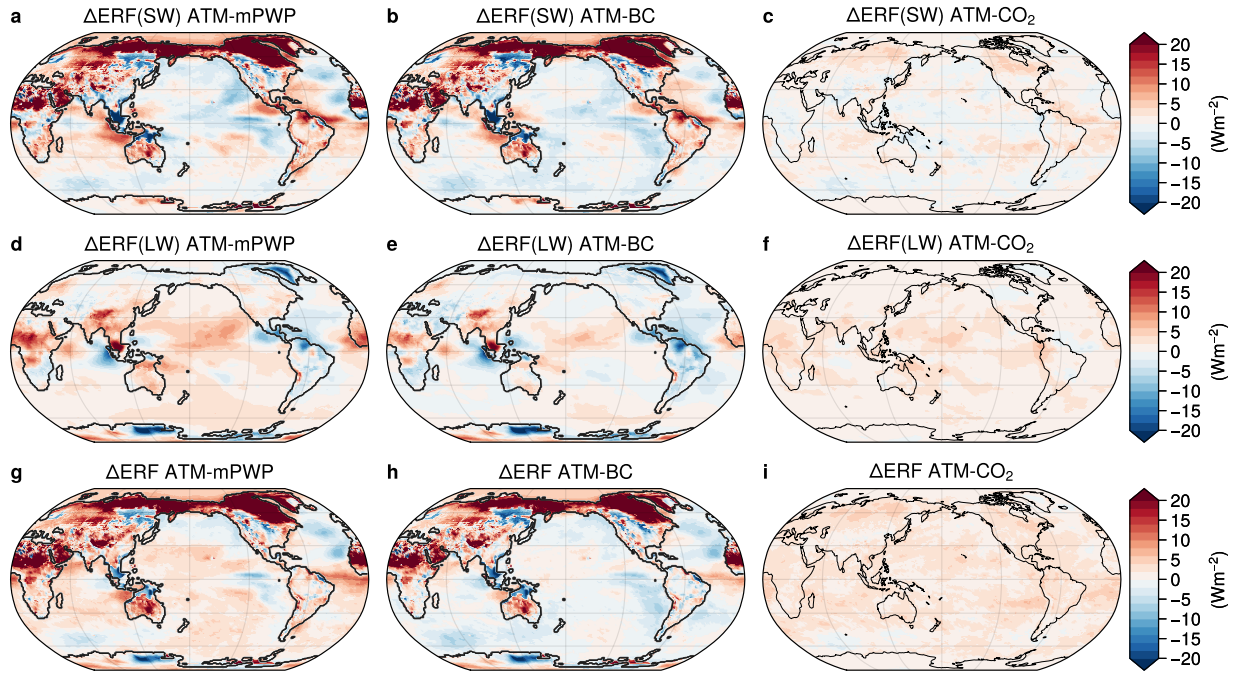


FIG. 3: Shortwave (a-c), longwave (d-f), and total (g-i) effective radiative forcing (ERF) anomalies diagnosed from top-of-atmosphere radiative imbalances in fixed-SST atmosphere-only (CAM6) simulations. All figures show ERF after making the global mean Hansen et al. (2005) adjustment (equation 2).

If boundary conditions and greenhouse gases affected global temperature in the same way, then each would induce warming in proportion to their fraction of the total mPWP ERF. The ERF from boundary condition changes in CESM2 is 1.7 Wm^{-2} (around 43% of the total mPWP forcing of 3.8 Wm^{-2}), while ERF from greenhouse gas changes in CESM2 is 2.2 Wm^{-2} (around 57% of the total mPWP forcing). However, we have shown that boundary condition changes alone contribute 55% of total mPWP warming in CESM2, while greenhouse gases contribute only 40% (with a remaining 5% coming from nonlinear interactions). While previous work has cast such differences in terms of varying forcing “efficacies” (e.g., Hansen et al. 2005; Zhu and Poulsen 2020), more recent work has shown that this is more naturally explained by the different spatial patterns of radiative forcing and the feedbacks that are induced (e.g., Zhou et al. 2023; Cooper et al. 2024). In particular, CO₂ forcing is relatively spatially uniform with a maximum in the tropics, while boundary condition forcing is spatially variable with the largest positive forcing at high latitudes and with some regions of negative forcing in the tropics (Fig. 3); these differences give rise to distinct patterns of SST

changes and feedbacks, and in turn to distinct global temperature responses. We examine these SST patterns in greater detail in the following section.

4. mPWP SST patterns and the role of ocean circulation changes

To better understand the respective contributions of CO₂ and boundary conditions to the mPWP global temperature response, we perform slab ocean simulations (CAM6 coupled to an ocean mixed layer of fixed depth) in which SSTs can change but ocean heat transport is fixed to that of CESM2's PI control simulation. By comparing the results of these simulations to the fully-coupled CESM2 simulations described above (Fig. 2), we can evaluate the role of ocean heat transport changes in shaping the SST response.

Using the CAM6 slab ocean model (SOM), we perform the same suite of five simulations as for the fully-coupled and atmosphere-only configurations described above (Table 1). We run the SOM simulations for a minimum of 70 years, with the average over the last ~50 used for analysis to avoid transient spin-up in the first couple of decades. All simulations show a TOA radiative imbalance of < 0.1 Wm⁻² at the end of run-time.

In each of these SOM simulations, mixed layer ocean heat flux convergence (qflux) is prescribed to match that of the seasonally-varying, fully-coupled CESM2 PI control climatology (e.g., Zhu and Poulsen 2021). Analogous to the fixed-SST simulations described above, regions of ocean that are retained in the mPWP simulations are given the PI qflux; in the region of new ocean grid cells of West Antarctica, where no PI qflux exists, the qflux is set to zero to reflect no ocean heat flux convergence in the PI control climatology (Supplementary Fig. S2). Nearest-neighbor interpolation is used to smooth the transition from zero qflux to PI control values, and a small residual is distributed across all grid cells in order to maintain a globally-integrated qflux of zero.

a. mPWP warming in the absence of ocean circulation changes

SOM-mPWP gives a globally-averaged surface warming of 4.5°C above the PI control, while SOM-BC and SOM-CO₂ give 1.2°C and 2.4°C of surface warming, respectively (Table 1). SOM-BC shows substantial Northern Hemisphere polar amplification, with warming over the North Pacific and North Atlantic Oceans and cooling over the tropical oceans; it also shows cooling over portions of the Southern Ocean (Fig. 4 b,e). In contrast, SOM-CO₂ shows a much more spatially

uniform SST response (Fig. 4 c,f), which is expected from the more-uniform pattern of radiative forcing (Fig. 3 i). Boundary conditions alone (SOM-BC) lead to less global warming per unit of forcing than does CO₂ alone (SOM-CO₂), and to much less warming than was seen in the corresponding fully-coupled simulation (FCM-BC) despite identical boundary conditions (Table 3). The small amount of warming in SOM-BC, despite a large ERF, indicates a more-negative (stabilizing) global feedback in response to boundary conditions than to CO₂ forcing. This is consistent with the increase in low-cloud cover in the eastern tropical Pacific Ocean and lack of low-cloud cover loss in the Southern Ocean in the SOM-BC simulation (Fig. 4 h), both of which act to reflect relatively more SW radiation than in the other simulations, resulting in less global warming.

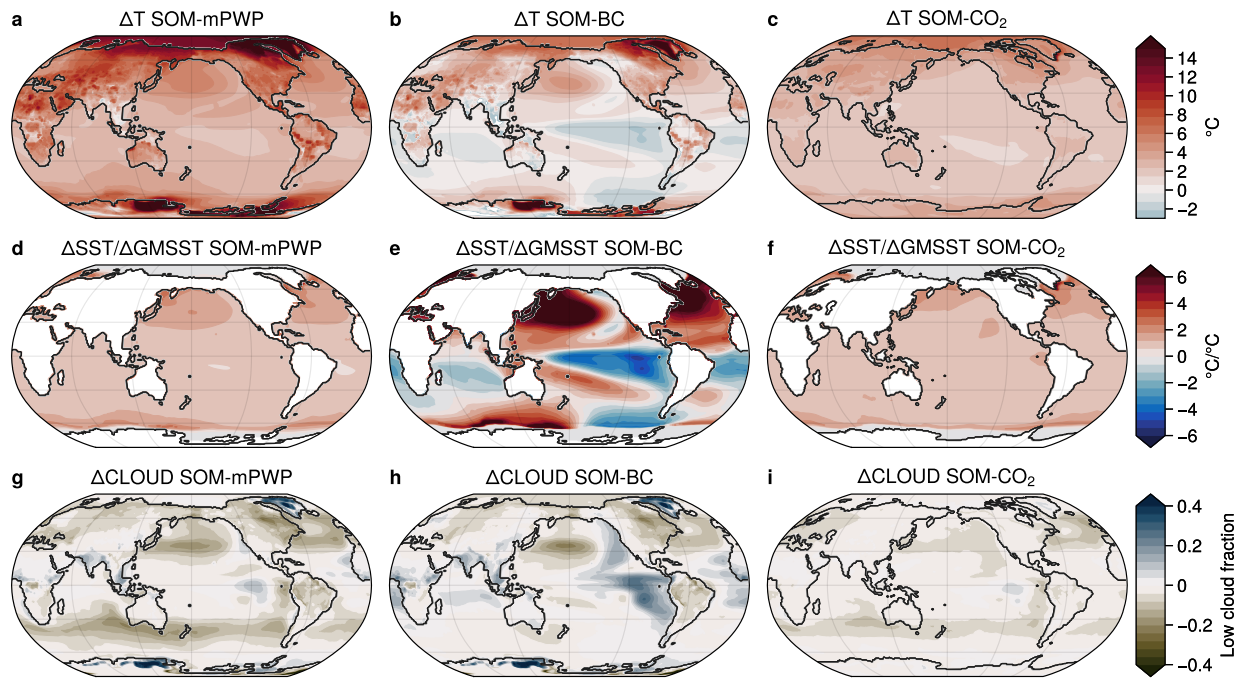


FIG. 4: Surface air temperature (a-c), sea-surface temperature normalized by global mean (d-f), and low cloud fraction (g-i) anomalies from preindustrial diagnosed slab ocean CESM2 simulations of mid-Pliocene forcings (SOM-mPWP), changes in boundary conditions only (SOM-BC), and changes in CO₂ only (SOM-CO₂).

The cause of these low-cloud cover changes in SOM-BC appears to be the cooling of the Southern Ocean in response to West Antarctic ice sheet changes. The atmospheric response to a lowering of the ice sheet topography is a cyclonic wind anomaly that advects cold polar air and sea ice

northward (Fig. 5), resulting in cooling of the Pacific sector of the Southern Ocean via a sea-ice-albedo feedback. These wind and SST anomaly patterns are consistent with those seen in a previous study of the response of slab ocean models to a lowering of West Antarctic topography (Steig et al. 2015).

The prominent surface cooling and low-cloud growth over the tropical east Pacific Ocean in SOM-BC is consistent with recent work demonstrating a southeast tropical Pacific cooling response to Southern Ocean cooling via an atmospheric teleconnection (Dong et al. 2022; Hartmann 2022; Kim et al. 2022; Kang et al. 2023b), in which advection of Southern Ocean cold air anomalies toward the equatorial Pacific by climatological winds initiates cooling in the southeast Pacific, enhanced by a wind-evaporation-SST (WES) feedback associated with a strengthening of southeasterly winds; in turn, surface cooling stabilizes the atmospheric boundary layer aloft, resulting in an increase in subtropical low-cloud cover that further amplifies surface cooling. We hypothesize that the same mechanism is at play here. This cooling of the Southern Hemisphere relative to the Northern also results in a large northward shift of the Intertropical Convergence Zone (ITCZ) in SOM-BC, which may further act to enhance southeast tropical Pacific cooling via a strengthening of the Hadley cell and an increase in surface winds. The negative SW ERF over the tropical Pacific Ocean in SOM-BC (Fig. 3 b) may also contribute to tropical cooling, though this appears to be a secondary effect given that the same ERF is present in all mPWP boundary condition simulations (Fig. 3 b) while tropical cooling only arises when the Southern Ocean cools as well (i.e., in SOM-BC).

The resulting increase in subtropical low-cloud cover and associated eastern Pacific cooling significantly reduces the global mean temperature response in SOM-BC. Interestingly, while the boundary condition and CO₂-driven ERFs were found to add linearly to the full mPWP ERF, globally-averaged temperature responses in the slab ocean simulations do not. This nonlinearity could arise from: (i) Southern Ocean sea ice loss under CO₂ forcing precluding a strong sea-ice-albedo feedback (and subsequent Southern Ocean cooling) in response to West Antarctic ice sheet changes in the absence of anomalous ocean heat transport; and (ii) asymmetries in the subtropical cloud response that have been shown to result in (locally) less-negative cloud feedbacks in areas of subtropical cooling as opposed to warming (Bloch-Johnson et al. 2024).

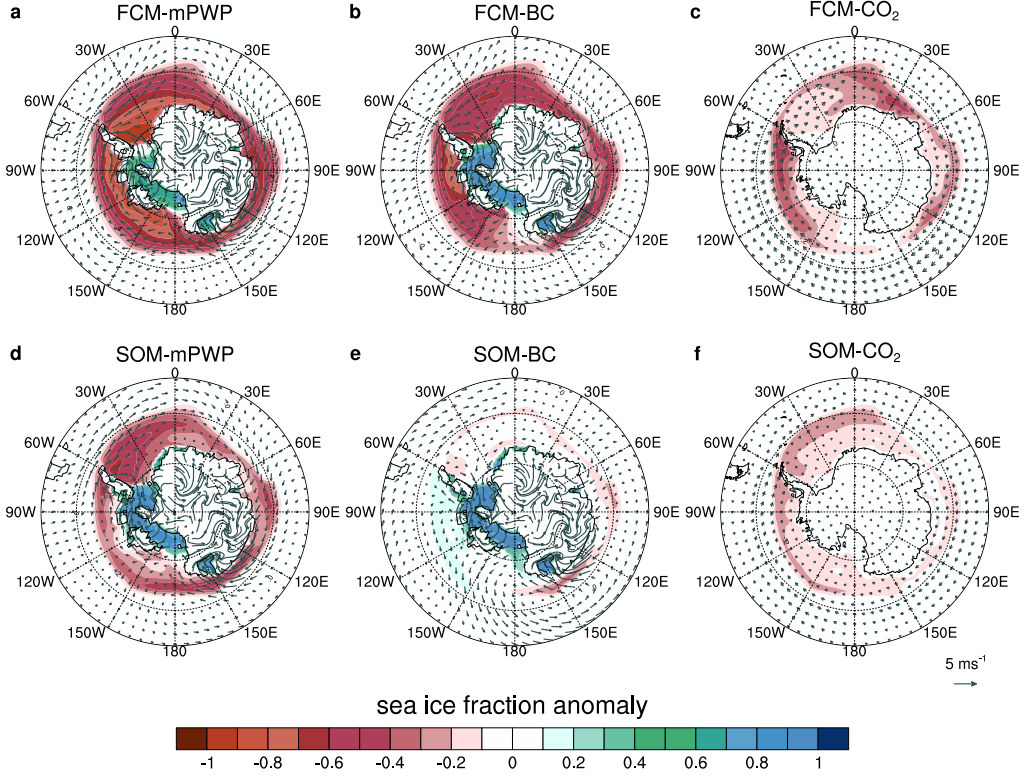


FIG. 5: Southern Ocean sea ice fraction anomalies for fully-coupled (a-c) and slab ocean (d-f) simulations, with surface wind anomalies indicated as vectors.

b. The role of ocean circulation changes in mPWP warmth

We now return to the fully-coupled CESM2 simulations to assess how ocean circulation changes influence the magnitude and spatial pattern of warming in response to mPWP forcings. Total warming in FCM-mPWP is approximately 5.1°C , or an increase of 0.6°C over SOM-mPWP, while FCM-BC and FCM-CO₂ produce 1.6°C more, and 0.4°C less, warming than their SOM equivalents, respectively. This highlights an important role for ocean circulation changes in enhancing the global temperature response to mPWP boundary conditions.

We find that the Southern Ocean and eastern tropical Pacific cooling seen in SOM-BC does not arise in FCM-BC, despite identical boundary conditions (compare Fig. 4 b and 2 b). Instead, FCM-BC shows strong Southern Ocean warming, which then by the same atmospheric teleconnections discussed above acts to warm the eastern tropical Pacific, resulting in a strong loss of subtropical low-cloud cover and an amplification of the global warming response. FCM-BC shows only a

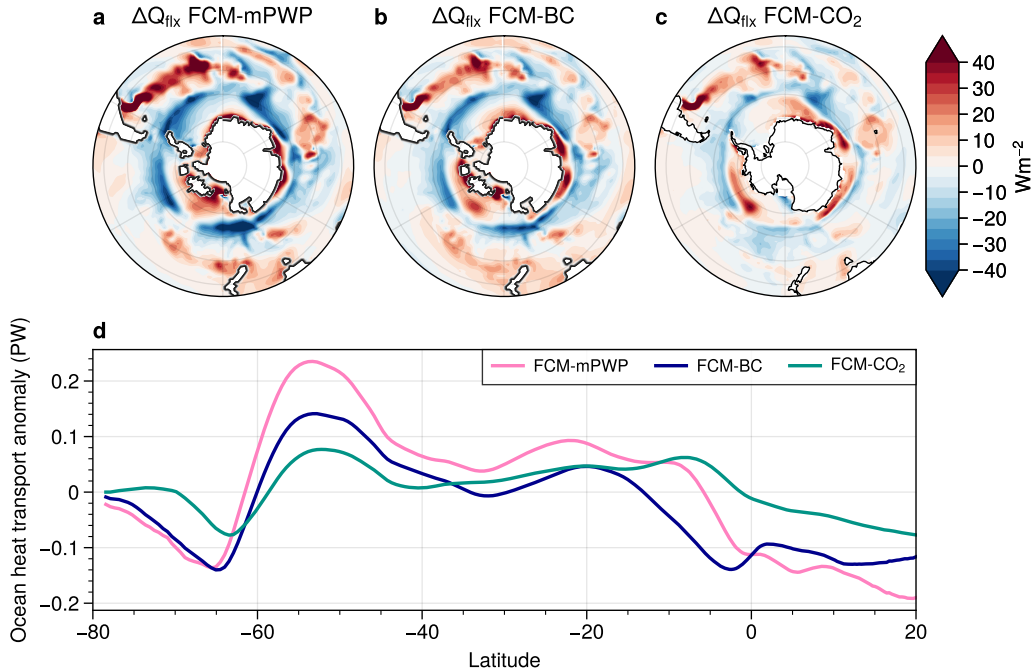


FIG. 6: Southern Ocean heat flux convergence (q_{flux}) anomalies calculated from fully-coupled simulations as the sum of the total surface heat flux and the internal latent heat of ice formation/melt into the mixed layer (a-c); zonal-average ocean heat transport anomalies from the same simulations (positive is northward) (d).

small northward shift of the ITCZ (Supplementary Fig. S3) – in part due to a weak hemispheric warming contrast given strong Southern Ocean warming, and in part due to anomalous southward cross-equatorial ocean heat transport reducing the need for the ITCZ to move northward from energy balance arguments (e.g., Green and Marshall 2017). Altogether, these differences result in much stronger warming of the eastern tropical Pacific in FCM-BC relative to SOM-BC.

Similar widespread warming of the Southern Ocean and tropical Pacific was also found by Steig et al. (2015) when using fully-coupled models in which ocean circulation was allowed to adjust in response to a lowering of the West Antarctic ice sheet. Steig et al. (2015) speculated that the relevant changes in Southern Ocean circulation could be a result of enhanced Ekman upwelling of relatively warm water associated with the cyclonic wind anomalies present over the eastern Pacific Southern Ocean. However, we find that the mPWP and boundary condition simulations do not show an increase in wind stress curl around Antarctica poleward of the Antarctic Circumpolar Current, as would be expected for enhanced upwelling (Supplementary Fig. S4).

Yet, we do find a strong increase in poleward ocean heat transport south of 65°S on the order of 0.1 PW in FCM-BC and FCM-mPWP (Fig. 6 a), consistent with an increase in ocean heat flux convergence in the West Antarctic, particularly at very high latitudes (Fig. 6 b). Note that 0.1 PW corresponds to heat flux convergence of around 4 Wm^{-2} averaged over the polar cap poleward of 65°S, which is larger than the average mPWP ERF values in this region (Fig. 3), illustrating why these ocean heat transport changes are such a substantial driver of southern high latitude warming and, in turn, on tropical and global warming through low-cloud feedbacks.

Enhanced Southern Ocean warming in FCM-mPWP was found to be common across models participating in PlioMIP2 (Weiffenbach et al. 2023), and was associated with dramatic sea ice loss and a decline in abyssal Southern Ocean overturning due to enhanced stratification. We also find significant warming of the water column in FCM-mPWP (Supplementary Fig. S5), and a decline in sea ice extent that is much more marked in FCM-mPWP and FCM-BC than FCM-CO₂ (Fig. 5 g-i), indicating a smaller role for CO₂ in driving sea ice loss and surface warming during the mPWP. The change in sign from cooling to warming in the eastern tropical Pacific in FCM-BC relative to SOM-BC provides evidence that the negative SW ERF there (Fig. 3 b,h) is not sufficient to drive tropical Pacific cooling in the presence of Southern Ocean warming.

To better isolate the climatic effect of Southern Ocean warming, we perform an additional slab ocean simulation in which we modify the qflx field in the Southern Ocean south of 65°S to reproduce FCM-BC ocean heat transport changes in only this region. Specifically, all ocean grid cells south of this latitude were prescribed to match the ocean heat flux convergence and mixed layer depth simulated in the last 50 year average of FCM-BC; PI qflx is retained elsewhere. The results show strong Southern Ocean warming that extends to the tropics in all ocean basins, resulting in a reduction in subtropical low-cloud cover and larger global warming, broadly consistent with FCM-BC (Supplementary Fig. S6). This indicates that Southern Ocean heat transport changes (Supplementary Fig. S7) alone are sufficient to produce the differences between fully-coupled model and slab ocean model responses to mPWP boundary condition forcing, and are the main reason for the larger global warming response in FCM-BC compared to SOM-mPWP. We note that a similarly important role for ocean dynamics in changing Southern Ocean and equatorial SSTs has been found in LGM simulations (Zhu and Poulsen 2021).

An evaluation of the slab ocean model biases (Supplementary Fig. S8) in both the PI and mPWP simulations suggests that up to 2°C of Southern Ocean temperature increases in the slab ocean simulations may be due to a methodological bias in this model set-up (e.g., resulting from using annual-mean mixed layer depths in the SOM versus seasonally-varying mixed layer depths in the FCM). However, this is a relatively small fraction (less than 10%) of the regional warming simulated in FCM-mPWP relative to SOM-mPWP, meaning that the Southern Ocean warming response in the fully-coupled model can be attributed to ocean heat transport changes.

To what degree do ice sheet changes drive the Southern Ocean warming of the mPWP, relative to all other boundary conditions? To answer this, we examine an existing fully-coupled CESM2 simulation that uses mPWP continental topography and ocean bathymetry, including a closed Bering Strait and exposed Sunda and Sahul shelves, but PI control ice sheet extent, vegetation, and CO₂-levels (including PI topography in Antarctica) (Eo280 in Feng et al. 2022; here referred to as FCM-Oro). We find that this simulation shows no Southern Ocean warming (Supplementary Fig. S9) and a global temperature anomaly of -0.6°C relative to the PI. These results suggest a leading role for West Antarctic ice sheet loss in driving Southern Ocean warming, in turn resulting in eastern tropical Pacific warming, a reduction in subtropical low-cloud cover, and an amplification of the global temperature response to mPWP forcings. Further work would be needed to unambiguously attribute Southern Ocean heat transport and temperature changes to West Antarctic ice sheet loss, rather than to other boundary condition changes that could remotely affect the region (namely changes in northern hemisphere vegetation and the Greenland ice sheet).

5. mPWP radiative feedbacks

Thus far we have found that boundary conditions – primarily associated with ice sheet loss – have an outsized influence on global temperature response of the mPWP. Here, we use our values of ERF and equation (1) to quantify the global radiative feedback, λ , for each slab ocean and fully-coupled simulation described above (Table 3). We also apply equation (1) to all-sky and clear-sky radiation fields separately to estimate the respective role of cloud feedbacks – here approximated by the Cloud Radiative Effect (CRE) per degree of warming. We note that a more sophisticated method using radiative kernels or perturbations would be necessary to account for effects such as cloud masking of water vapor, lapse rate, and surface albedo changes in the calculation of a cloud

feedback (Soden et al. 2004); it is, however, a good approximation where surface albedo changes are small (over open ocean).

As expected, we find that the global feedback associated with mPWP boundary conditions differs from that associated with CO₂ within both slab ocean and fully-coupled simulations. Within the former, boundary conditions drive a far more negative feedback ($\lambda_{BC} = -1.42 \text{ Wm}^{-2}\text{K}^{-1}$ in SOM-BC) than does CO₂ ($\lambda_{CO_2} = -0.80 \text{ Wm}^{-2}\text{K}^{-1}$ in SOM-CO₂), consistent with boundary conditions inducing a subtropical cooling and low-cloud cover increase not seen under CO₂ forcing. However, we find the opposite behavior within the fully-coupled model: boundary conditions drive a far less negative feedback ($\lambda_{BC} = -0.59 \text{ Wm}^{-2}\text{K}^{-1}$ in FCM-BC) than does CO₂ ($\lambda_{CO_2} = -1.01 \text{ Wm}^{-2}\text{K}^{-1}$ in FCM-CO₂), consistent with increased poleward ocean heat transport to the southern high latitudes resulting in Southern Ocean warming and a subsequent decrease in subtropical cloud cover.

TABLE 3: Global radiative feedbacks calculated as in equation (1). The period of analysis, ΔN , and ΔT values for each simulation are as noted in Table 1.

	$\Delta N (\text{Wm}^{-2})$	$\Delta F (\text{Wm}^{-2})$	$\Delta T (\text{K})$	$\lambda (\text{Wm}^{-2}\text{K}^{-1})$
FCM-mPWP	0.25	3.83	5.10	-0.70
FCM-BC	0.03	1.65	2.85	-0.59
FCM-CO ₂	0.14	2.17	2.01	-1.01
FCM-2xCO ₂	0*	4.53	4.07*	-1.12*
SOM-mPWP	0.08	3.83	4.46	-0.84
SOM-BC	0.02	1.65	1.15	-1.42
SOM-CO ₂	-0.03	2.17	2.41	-0.91
SOM-2xCO ₂	0.09	4.53	5.56	-0.80

*corresponds to a regression of ΔN on ΔT over years 100-300, with the equilibrium temperature extrapolated to $\Delta N = 0 \text{ Wm}^{-2}$.

The spatial patterns of radiative feedbacks (defined as the local top-of-atmosphere radiative response per degree of global surface temperature change), help to explain why the boundary conditions drive a small global temperature response in the slab ocean model: a strong negative cloud feedback over areas of surface cooling in the eastern subtropical Pacific – a pattern that is reversed in the fully-coupled model (Fig. 7 b,e,h). Note that in all simulations, the subtropical Pacific cloud feedback is locally positive (amplifying local surface temperature changes); therefore, when quantified in terms of a global temperature change, the change in sign between model configurations (Figs. 7 and 8) stems from the subtropical Pacific cooling in SOM-BC resulting in a local increase in low-cloud cover despite global warming, and from the subtropical Pacific warming

in FCM-BC resulting in a local decrease in low-cloud cover with global warming. Furthermore, relatively larger warming in the Southern Ocean, subtropical Pacific Ocean, and North Atlantic Ocean in FCM-BC and FCM-mPWP corresponds to a more-positive cloud feedback in these regions, resulting in an overall feedback that is less negative under boundary conditions than CO₂.

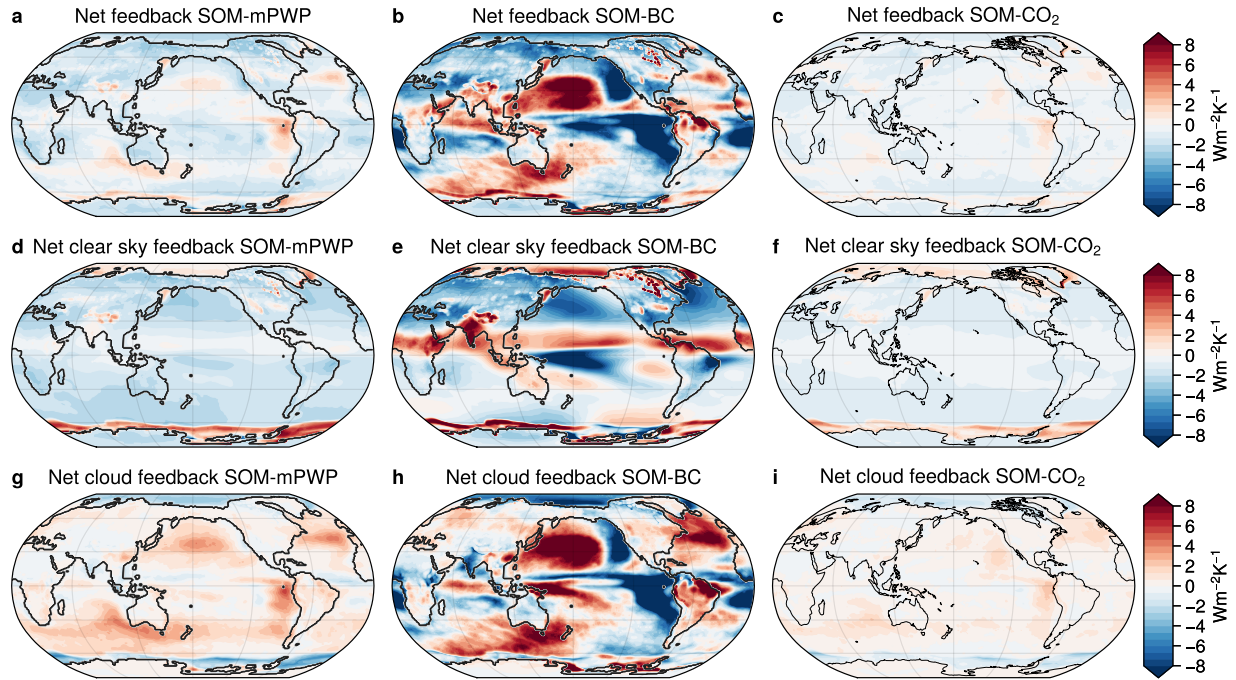


FIG. 7: Net (a-c), clear sky (d-f), and cloud (g-i) radiative feedbacks from slab ocean simulations, calculated using equation (1) and normalized by the global mean surface air temperature response. The cloud feedback is calculated using the difference between all-sky and clear-sky TOA radiative imbalance anomalies (CRE per degree of warming).

The global feedback of the mPWP (λ_{mPWP}) can be understood as a weighted sum of λ_{BC} and λ_{CO_2} separately. This can be seen by applying equation (1) to each simulation separately and allowing for different feedbacks; at equilibrium this gives $\Delta T_{\text{mPWP}} = -\Delta F_{\text{mPWP}} / \lambda_{\text{mPWP}}$, $\Delta T_{\text{CO}_2} = -\Delta F_{\text{CO}_2} / \lambda_{\text{CO}_2}$, and $\Delta T_{\text{BC}} = -\Delta F_{\text{BC}} / \lambda_{\text{BC}}$. Assuming global temperature response (and ERF) sums linearly for these simulations – a good approximation for the fully-coupled model – we can approximate $\Delta T_{\text{mPWP}} = \Delta T_{\text{CO}_2} + \Delta T_{\text{BC}}$ and $\Delta F_{\text{mPWP}} = \Delta F_{\text{CO}_2} + \Delta F_{\text{BC}}$. From equation (1) applied at equilibrium,

the global feedback under full mPWP forcing can then be written as

$$\begin{aligned}\lambda_{\text{mPWP}} &= -\frac{\Delta F_{\text{mPWP}}}{\Delta T_{\text{mPWP}}}, \\ &\approx \lambda_{\text{CO}_2} \frac{\Delta T_{\text{CO}_2}}{\Delta T_{\text{mPWP}}} + \lambda_{\text{BC}} \frac{\Delta T_{\text{BC}}}{\Delta T_{\text{mPWP}}}.\end{aligned}\quad (3)$$

That is, the mPWP feedback is the sum of the feedbacks under CO_2 alone and boundary conditions alone, weighted by the respective fractional contributions of those scenarios to total mPWP warming. From values in Table 2, equation (3) provides an estimate $\lambda_{\text{mPWP}} \approx -0.73 \text{ Wm}^{-2}\text{K}^{-1}$, in good agreement with the actual value of $\lambda_{\text{mPWP}} = -0.70 \text{ Wm}^{-2}\text{K}^{-1}$ derived from equation (1) applied to the fully-coupled mPWP simulation. Equation (3) shows why the value of λ_{mPWP} must be between the values of λ_{CO_2} and λ_{BC} , and why λ_{mPWP} is closer to λ_{BC} in the fully-coupled model (because ΔT_{BC} is larger than ΔT_{CO_2}). Equation (3) does not provide an accurate estimate of λ_{mPWP} in the slab ocean model, where the assumption of linearity does not hold, but it still provides qualitative reasoning for why λ_{mPWP} is close to λ_{CO_2} in the slab ocean model (because ΔT_{CO_2} is much larger than ΔT_{BC}).

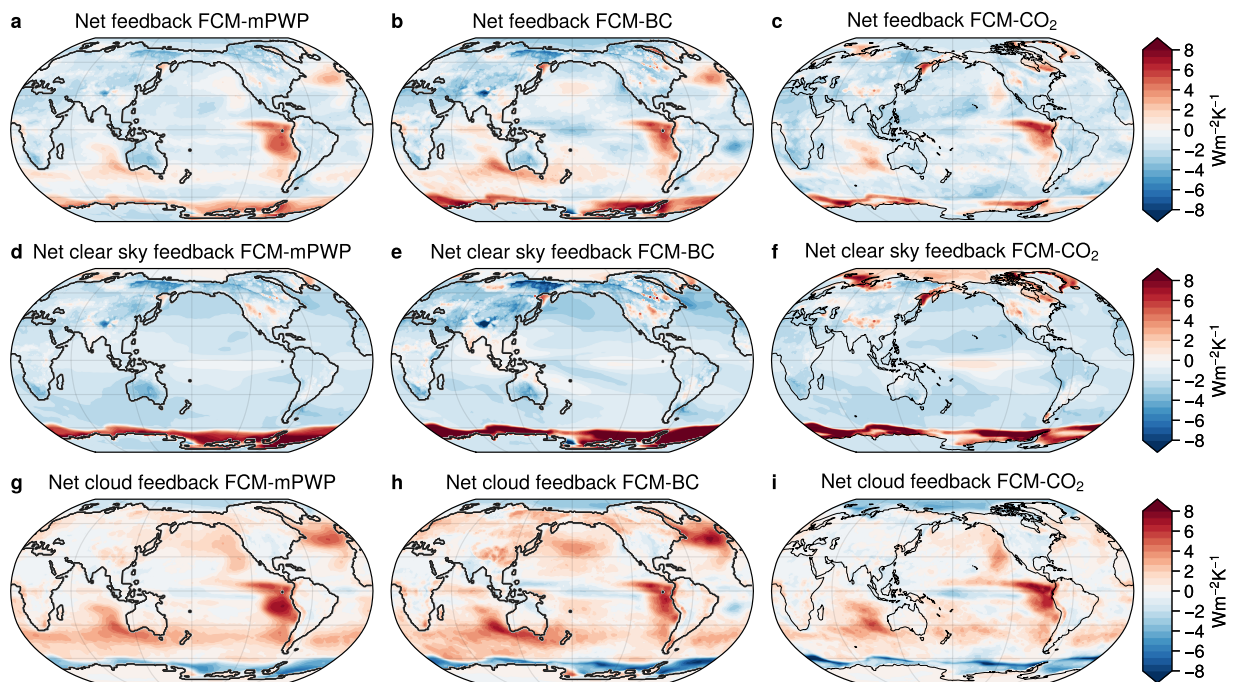


FIG. 8: As in Fig. 7, but for fully-coupled simulations.

To what extent do feedbacks operating during the mPWP represent a good analog to those operating under greenhouse gas forcing today? Some mPWP-like boundary conditions (e.g., ice sheet and vegetation changes) can be expected to occur slowly over the coming centuries, while other mPWP-like boundary conditions (e.g., changes in land topography and ocean bathymetry) are not expected to occur in the same way even in the distant future. It is therefore important to quantify the extent to which λ_{mPWP} differs from the feedback governing near-term warming in the absence of these boundary conditions. To do so, we calculate the difference between λ_{mPWP} and an estimate of the global feedback under abrupt CO₂ doubling (Tables 1 and 3), $\lambda_{2x\text{CO}_2}$, as:

$$\Delta\lambda = \lambda_{2x\text{CO}_2} - \lambda_{\text{mPWP}}. \quad (4)$$

We interpret $\Delta\lambda$ as primarily reflecting different patterns of surface warming induced by the unique boundary conditions of the mPWP (which are not expected to occur in the near-term future) and induced by modern-day CO₂ forcing. We can then infer that $\Delta\lambda$ represents a paleoclimate ‘pattern effect’, following other recent studies (e.g., Cooper et al. 2024). $\Delta\lambda$ has been widely estimated for the historical record, during which greater warming has been observed in the western tropical Pacific than the eastern tropical Pacific, enhancing deep convection and increasing tropospheric stability, and thus producing more negative (stabilizing) cloud feedbacks (Dong et al. 2019; Andrews et al. 2018, 2022) – an SST pattern that is expected to reverse with greenhouse-gas driven future warming, driving less-negative feedbacks (Ceppi and Gregory 2017; Dong et al. 2019; Forster et al. 2021). Equation (4) provides a quantification of this SST pattern effect for the mPWP.

We compare the global feedback under mPWP forcing to the feedback under an abrupt CO₂ doubling, which defines ECS when equilibrium warming is reached. ECS has been found to be highly correlated with warming over the 21st century within climate models (e.g., Sherwood et al. 2020). Although we have extended fully-coupled CESM2’s abrupt CO₂ doubling simulation (FCM-2xCO₂) to a length of 300 years, it is still far from equilibrium at the end of runtime. We therefore calculate ECS as the equilibrium temperature change extrapolated from a Gregory regression following Gregory et al. 2004 (producing an ECS of approximately 4.1°C; see Table 3 and footnote therein; Supplementary Fig. S10). We then calculate $\lambda_{2x\text{CO}_2} = -F_{2x\text{CO}_2}/\text{ECS}$, where $F_{2x\text{CO}_2}$ is the ERF quantified using a fixed-SST simulation as described in Section 3 (Table 3). For the slab ocean model, we perform a CO₂ doubling simulation (SOM-2xCO₂) that reaches

equilibrium, allowing us to quantify ECS directly as the global average temperature anomaly (producing an ECS of approximately 5.6°C; Tables 1 and 3).

The difference between ECS values in slab ocean and fully-coupled versions of CESM2 may reflect differences in ocean heat transport between the two configurations. Our estimate of ECS in the slab ocean version of CESM2 (5.6°C) is slightly higher than the widely-cited estimate of 5.1–5.3°C, which has been derived from previous 2xCO₂ SOM simulations (Danabasoglu et al. 2020; Gettelman et al. 2019; Zelinka et al. 2020), but identical to the most recent estimate using the same model configuration (Zhu et al. 2021). On the other hand, our estimate of ECS in the fully-coupled CESM2 (4.1°C) is substantially lower than widely-cited estimates of ECS estimated from abrupt CO₂ quadrupling simulations with CESM2 (> 5°C) but higher than estimates based on regression over the previously-available 150 years of abrupt CO₂ doubling (e.g., 3.4°C in Poletti et al. 2024). Our 2xCO₂ ERF estimate of 4.5 Wm⁻² is greater than 1/2 the value of published estimates of 4xCO₂ ERF (6.7 Wm⁻², Poletti et al. 2024; 8.9 Wm⁻², Smith et al. 2020). We can therefore infer that the difference we find in ECS is associated with greater sensitivity of CESM2 at higher global warming levels, rather than non-logarithmic behavior of CO₂ forcing with concentration (Poletti et al. 2024; Rugenstein and Armour 2021; Bloch-Johnson et al. 2021). Our estimate of ECS of 4.1°C, based on a 300 year-long simulation of CO₂ doubling, is consistent with the 900 year FCM-CO₂ simulation scaled logarithmically to a higher CO₂ level (4.1°C), and likely represents the current most accurate estimate of ECS for CESM2.

We calculate a pattern effect, $\Delta\lambda$, equal to $-0.07 \text{ Wm}^{-2}\text{K}^{-1}$ in our slab ocean model, but $-0.4 \text{ Wm}^{-2}\text{K}^{-1}$ in the fully-coupled. That is, feedbacks induced by mPWP forcings are substantially less negative than feedbacks induced by CO₂ doubling alone in the fully-coupled model. This large value of $\Delta\lambda$ in the fully-coupled model reflects the fact that mPWP boundary conditions, hypothesized here to be associated with the response of ocean circulation to ice sheet loss, induce less-negative feedbacks primarily via the cloud changes described above (Fig. 8). That we find such an important role for subtropical cloud cover in the warming of the mPWP is consistent with previous work identifying, through energy balance analysis, a decrease in cloud albedo in the Southern Hemisphere subtropics across the PlioMIP2 ensemble (Burton et al. 2023); it is also supported by research demonstrating that subtropical cloud albedo reductions alone can enhance regional surface temperatures sufficient to reproduce reconstructed tropical Pacific SSTs of the

mPWP (Burls and Fedorov 2014). In the following section, we discuss the implications of these findings for estimates of the modern-day ECS based on mPWP reconstructions.

6. Discussion

Efforts to constrain ECS and future warming from paleoclimate records often make the implicit assumption that the climate response to paleoclimate forcing is analogous to that associated with today's greenhouse gas forcing. Recent research leveraging both models (Zhu and Poulsen 2021) and data assimilation approaches (Cooper et al. 2024) suggests that this may not be a good assumption for the LGM. In particular, the response to LGM ice sheet forcing was found to be characterized by less-negative radiative feedbacks than the response to CO₂ forcing due to the distinct spatial patterns of temperature change they induce, referred to in the literature as the “pattern effect”. The implication is that more of the LGM cooling may have come from ice sheet forcing, rather than CO₂, than previously recognized. Thus, high values of ECS (measuring global temperature response to CO₂ forcing alone) are inconsistent with reconstructed LGM cooling (Cooper et al. 2024).

Motivated by these findings, we evaluated the potential for mPWP boundary condition forcing to produce a different climate response than CO₂ forcing. By performing novel fixed-SST simulations with CESM2, we quantified the ERF of mPWP boundary condition and CO₂ changes. Our estimates can be compared to the mPWP forcing estimates used in the community ECS assessment of Sherwood et al. (2020) (hereafter SW20). Here, total greenhouse gas (including methane and nitrous oxide) forcing was found to be 2.2 Wm⁻² – identical to our mPWP CO₂ ERF estimate of 2.2 Wm⁻². As in Haywood et al. (2016), we interpret our CO₂ forcing (corresponding to 400 ppm rather than 375 ppm as in SW20) as representative of the total greenhouse gas forcing of the mPWP. SW20 represented boundary condition forcing by applying an additional inflation factor to the greenhouse gas forcing to arrive at a central estimate of total mPWP of 3.3 Wm⁻², or 0.5 Wm⁻² smaller than our estimate of 3.8 Wm⁻². Because the greenhouse gas forcing estimates are nearly identical, the difference in total mPWP forcing comes from our value of boundary condition ERF being 0.5 Wm⁻² larger than the central estimate implied in SW20.

Our higher value of mPWP boundary condition forcing may reflect our use of a single climate model (CESM2), or our use of the modern ERF definition, which allows for rapid atmospheric

adjustment to forcing (increasing ERF relative to instantaneous radiative forcing, for example). We note that it is unclear how corrections to ERF (to remove the effect of land surface temperature changes on top-of-atmosphere radiation) should be applied for non-CO₂ forcings, such as ice sheet or vegetation changes, that are localized over land and induce significant local temperature change. Here we have simply followed common practice (Andrews et al. 2021) via equation (2), which results in a slight increase in our estimate of ERF. Not adjusting for this surface temperature change would decrease our estimate of total forcing by about 0.3 Wm⁻², bringing it closer to the SW20 forcing estimate but also increasing our pattern effect estimate from $-0.4\text{Wm}^{-2}\text{K}^{-1}$ to $-0.5\text{Wm}^{-2}\text{K}^{-1}$. Use of the adjusted ERF therefore provides a slightly more conservative estimate of the mPWP pattern effect in CESM2.

It would be valuable to perform similar 30-year simulations with fixed-SSTs in other atmospheric models to inform future mPWP forcing estimates, and to quantify each of the various forcings individually. Inclusion of fixed-SST simulations in the next PlioMIP, for example, would allow for an estimation of intermodel spread in mPWP forcings and feedbacks.

a. Implications for estimating ECS

To the extent that mPWP-like boundary condition (i.e., ice sheet and vegetation) changes will occur in response to modern greenhouse gas warming, they will do so slowly. We can therefore expect them to have little impact on the climate in the near-term (i.e., over this century), but a potentially large impact on timescales of multiple centuries to millennia (PALEOSENS 2012; Knutti and Rugenstein 2015) And while there is no strict separation of timescales allowing one to disregard these slower feedbacks, they are not typically included in estimates of modern-day ECS. In Section 5, we found the difference between the global feedback relevant to future warming ($\lambda_{2x\text{CO}_2}$) and to the mPWP (λ_{mPWP}) to be $-0.4\text{ Wm}^{-2}\text{K}^{-1}$ within CESM2, due to differences in the spatial pattern of warming resulting in a less-negative feedback under full mPWP forcing. The common assumption that the feedbacks at the mPWP are similar to those under greenhouse gas forcing today ($\lambda_{2x\text{CO}_2} \approx \lambda_{\text{mPWP}}$, or $\Delta\lambda = 0$) would therefore bias estimates of ECS upward (toward a too-sensitive climate). However, this can be corrected for by accounting for these feedback differences (Cooper et al. 2024).

To illustrate this principle, we consider the mPWP-constrained likelihood of ECS following the methods of SW20. In particular, to infer the modern-day ECS from mPWP evidence, we have

$$\begin{aligned} \text{ECS} &= -\frac{\Delta F_{2x\text{CO}_2}}{\lambda_{2x\text{CO}_2}}, \\ &= -\frac{\Delta F_{2x\text{CO}_2}}{\lambda_{\text{mPWP}}^* + \Delta\lambda}, \end{aligned} \quad (5)$$

where λ_{mPWP}^* is the estimate of the mPWP feedback determined using equation (1) applied to the mPWP at equilibrium. That is,

$$\lambda_{\text{mPWP}}^* = -\frac{\Delta F_{\text{mPWP}}^*}{\Delta T_{\text{mPWP}}^*}, \quad (6)$$

where ΔF_{mPWP}^* is an estimate of mPWP forcing and ΔT_{mPWP}^* is the mPWP global temperature change from proxy reconstructions. If we take ΔF_{mPWP}^* and ΔT_{mPWP}^* from SW20 (Supplementary Information) and set $\Delta\lambda = 0$, then the likelihood for ECS reproduces that in SW20 with a maximum likelihood of 3.2 K and a long tail toward high values (Fig. 9). Updating the SW20 likelihood function to match the latest proxy-based assessment of $\Delta T_{\text{mPWP}}^* = 3.9 \text{ K} \pm 1.1 \text{ K}$ (one sigma; Annan et al. 2024) increases this estimate of ECS to 4.2 K (solid black line in Fig. 9).

Next, we illustrate the effect of also updating the mPWP forcing to match the values estimated using the ERF in this study. Our results suggest a value of ΔF_{mPWP} that is about 0.5 W m^{-2} larger than the central value of ΔF_{mPWP}^* used in SW20 (Section 3) due to a different estimate of mPWP boundary condition forcing. Although our estimate of ΔF_{mPWP} is from a single model (CESM2), it represents the first quantification of the ERF for the mPWP. To illustrate the impact of the larger forcing, we maintain the uncertainty in the original SW20 value of ΔF_{mPWP}^* , but increase its median value by 0.5 W m^{-2} . This change produces a maximum likelihood for ECS that is slightly lower than the updated SW20 estimate (green line in Fig. 9).

Finally, we revise ΔF_{mPWP}^* to match our CESM2 value while also accounting for our CESM2-estimated value of $\Delta\lambda$ (Eq. 5). This produces a maximum likelihood of 2.8 K with much smaller likelihood of high values (purple curve in Fig. 9). This illustrates how accounting for feedback differences between the mPWP and modern-day CO₂-induced warming, in the absence of slow boundary condition changes, has the potential to produce estimates of ECS from mPWP evidence that are substantially lower and better constrained.

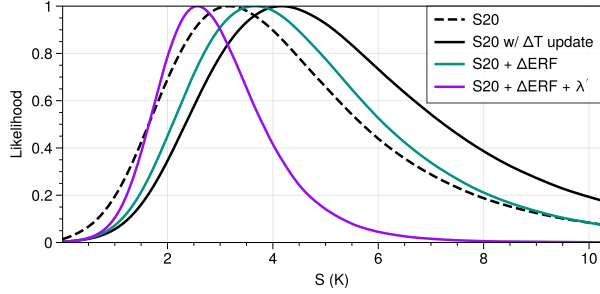


FIG. 9: Inference of modern-day climate sensitivity from the mPWP, reproduced from Sherwood et al. 2020 (dashed black line), updated based on latest-available proxy evidence (Annan et al. 2024) (solid black line), and then adjusted to account for enhanced boundary condition forcing found in this study (green line), as well as the mPWP pattern effect (purple line).

b. Implications for estimating ESS

Our results also have consequences for the estimation of Earth System Sensitivity (ESS), which captures the long-term (multi-centennial to multi-millennial) climate response to a doubling of CO₂. In this framing, large-scale ice sheet and vegetation changes are treated as additional feedbacks on warming in response to CO₂ forcing. Given the small impact that non-ice sheet related orographic changes (such as ocean gateway closures) and ocean bathymetric changes were found to have on the modeled mPWP climate in CESM simulations (Feng et al. 2017), the response to boundary condition forcing of the mPWP can be thought of as representing plausible changes that we may eventually see under modern-day greenhouse forcing (e.g., Haywood et al. 2013), with relevance to future climate on very long timescales.

From climate model simulations of mPWP warming, ESS can be estimated as $\text{ESS} \approx \Delta T_{\text{mPWP}} \cdot F_{2x\text{CO}_2}/F_{\text{CO}_2}$, where ΔT_{mPWP} is the warming from the full mPWP forcing and the factor $F_{2x\text{CO}_2}/F_{\text{CO}_2}$ is needed to convert to a warming from CO₂ doubling given that mPWP warming arose from a lower CO₂ level (e.g., Haywood et al. 2013). Thus, the ratio of ESS to ECS can be expressed as:

$$\frac{\text{ESS}}{\text{ECS}} \approx \frac{\Delta T_{\text{mPWP}}}{\text{ECS}} \cdot \frac{\Delta F_{2x\text{CO}_2}}{\Delta F_{\text{CO}_2}} \quad (7)$$

which for fully-coupled CESM2 gives a value of $\text{ESS/ECS} = 2.6$ (from values in Table 3). That is, as estimated by CESM2, the long-term warming from CO₂ doubling would be amplified by a

factor of 2.6 due to boundary conditions, relative to ECS. For example, given our mPWP-informed central estimate of 2.8 K (Fig. 9), this implies an ESS of 7.3 K – occurring on the timescale over which ice sheets and vegetation fully respond to and, in turn, amplify the warming. While this amplification factor is substantially higher than previous estimates of 1-2 (Haywood et al. 2013; Lunt et al. 2010, 2012), it is still within the bounds of the multi-model ensemble of PlioMIP2 (1.1-2.9) (Haywood et al. 2020).

What explains the high ESS/ECS ratio in CESM2? Using $\lambda_{2xCO_2} \approx \lambda_{CO_2}$ and $\Delta T_{mPWP} \approx \Delta T_{CO_2} + \Delta T_{BC}$ (good approximations for CESM2), equation (7) can be rewritten as:

$$\frac{ESS}{ECS} \approx 1 + \frac{\Delta F_{BC}}{\Delta F_{CO_2}} \cdot \frac{\lambda_{CO_2}}{\lambda_{BC}} \quad (8)$$

which gives a value of $ESS/ECS = 2.3$ – a decent approximation to the factor calculated directly from equation (7). When written this way, we can now interpret the ratio ESS/ECS in terms of two factors. The first ($\Delta F_{BC}/\Delta F_{CO_2}$) represents the ratio of boundary condition ERF to CO_2 ERF. If ΔF_{BC} were zero, then ESS would be equal to ECS. However, as we saw above, boundary condition ERF for the mPWP in CESM2 is larger than previous estimates (SW20). If we only consider this contribution by setting $\lambda_{CO_2} = \lambda_{BC}$ in equation (8), then ESS/ECS would be equal to only 1.8 – substantially smaller than the actual value of ESS/ECS, and in good agreement with previous estimates that assume a constant feedback across mPWP forcings (Haywood et al. 2013; Lunt et al. 2010). CESM2’s large value of ESS/ECS comes from the fact that a large ΔF_{BC} also induces a less-negative radiative feedback than does ΔF_{CO_2} such that the second factor ($\lambda_{CO_2}/\lambda_{BC}$) is large, altogether resulting in ESS/ECS well above 2.

It is possible that studies arriving at much lower values of ESS/ECS could have done so by overestimating ECS by neglecting to account for the pattern effect on radiative feedbacks (Hansen et al. 2023) or by relying on estimates using high CO_2 (e.g., quadrupling) simulations (e.g., Haywood et al. 2020 and citations therein). Generally speaking, where high latitude forcing results in high latitude temperature change (often referred to as a reduced meridional temperature gradient in the paleoclimate record (Forster et al. 2021)), less-negative feedbacks result; correcting for this implies a lower modern ECS when ice sheet forcing is small.

7. Conclusions

In this study, we found that mPWP boundary conditions were responsible for over half of the mPWP warming despite amounting to less than half of the mPWP ERF (Table 3). This implies that mPWP boundary conditions induce less-negative radiative feedbacks than does CO₂ (Table 3), consistent with their distinct spatial patterns of temperature and low-cloud responses (Fig. 2). We proposed that a primary reason for the less-negative cloud feedback under mPWP boundary condition forcing is increased poleward ocean heat transport in the Southern Ocean, resulting from a loss of the West Antarctic ice sheet. Warming of the Southern Ocean then enhances warming of the eastern tropical Pacific Ocean through an atmospheric teleconnection pathway that ultimately results in a reduction in subtropical low clouds, and thus a less-negative global feedback under boundary condition forcing.

It is possible that CESM2 overestimates the climate response to mPWP boundary conditions. This model is known to have a large subtropical cloud feedback, which strengthens the teleconnection between Southern Ocean warming and tropical Pacific warming (Kang et al. 2023a). However, CESM2 has been found to compare better than other climate models to observations of subtropical cloud properties (Kang et al. 2023b; Davis and Medeiros 2024). While the results shown here are surely model-dependent, they highlight a need to quantify the mPWP ERF within additional atmosphere-only models and to produce more robust estimates of ERF and $\Delta\lambda$ for the mPWP using both additional climate models and proxy-constrained data assimilation methods.

The results presented here have two important implications for future climate prediction. On the one hand, that so much of the mPWP warming may have come from non-CO₂ boundary conditions (inducing less-negative feedbacks via an SST pattern effect) suggests that near-term warming in the absence of these changes may be smaller than commonly reported. There exist opportunities to constrain mPWP warming patterns and feedbacks using proxy data assimilation, for example following similar methods to Cooper et al. (2024). Our results suggest that those efforts could lead to stronger constraints on the high end of ECS. On the other hand, they raise the possibility that ESS may be larger than commonly estimated, implying substantially higher global warming in the long term response to CO₂ as slow feedbacks (i.e., vegetation and ice sheet changes) materialize. Our results demonstrate the importance of incorporating these processes in projections of climate change.

Acknowledgments. The CESM project is supported primarily by the National Science Foundation (NSF). This material is based upon work supported by the National Center for Atmospheric Research (NCAR), which is a major facility sponsored by the NSF under Cooperative Agreement No. 1852977. This work was supported by National Science Foundation awards OCE-2002276 and AGS-1752796 (M.T.D., K.C.A., V.T.C.); AGS-2238875 and OCE-2103055 (R. F.); OCE-2002448 and AGS-1844380 (N.J.B.) National Oceanic and Atmospheric Administration MAPP Program award NA20OAR431039 (M.D., K.C.A., and C.P.); a Calvin Professorship in Oceanography (K.C.A.); and a Dept. of Defense NDSEG Fellowship (V.T.C.).

Data availability statement. Preindustrial control and mPWP fully-coupled CESM2 simulation outputs are available through the Earth System Grid Federation (<https://aims2.llnl.gov/search>) and are NCAR’s contribution to CMIP6. Atmosphere-only and slab ocean simulation outputs analyzed in this study, as well as the fully-coupled 2xCO₂ extension data, are stored on NCAR’s data repository; requests for access should be directed to Michelle Dvorak (mtdvorak@uw.edu). Requests for any other simulation outputs employing the mPWP boundary conditions should be directed to Ran Feng (ran.feng@uconn.edu).

References

- Andrews, T., J. M. Gregory, and M. J. Webb, 2015: The dependence of radiative forcing and feedback on evolving patterns of surface temperature change in climate models. *J. Climate*, **28** (4), 1630–1648.
- Andrews, T., C. J. Smith, G. Myhre, P. M. Forster, R. Chadwick, and D. Ackerley, 2021: Effective radiative forcing in a GCM with fixed surface temperatures. *J. Geophys. Res. Atmos.*, **126** (4), <https://doi.org/10.1029/2020JD033880>.
- Andrews, T., and Coauthors, 2018: Accounting for changing temperature patterns increases historical estimates of climate sensitivity. *Geophys. Res. Lett.*, **45** (16), 8490–8499.
- Andrews, T., and Coauthors, 2022: On the effect of historical SST patterns on radiative feedback. *J. Geophys. Res. Atmos.*, **127** (18), <https://doi.org/10.1029/2022JD036675>.

Annan, J. D., J. C. Hargreaves, T. Mauritzen, E. McClymont, and S. L. Ho, 2024: Can we reliably reconstruct the mid-Pliocene Warm Period with sparse data and uncertain models? *Climate of the Past*, **20** (9), 1989–1999.

Armour, K. C., C. M. Bitz, and G. H. Roe, 2013: Time-varying climate sensitivity from regional feedbacks. *J. Climate*, **26** (13), 4518–4534, <https://doi.org/10.1175/JCLI-D-12-00544.1>.

Baatsen, M. L., A. S. von der Heydt, M. A. Kliphuis, A. M. Oldeman, and J. E. Weiffenbach, 2021: Warm mid-Pliocene conditions without high climate sensitivity: the CCSM4-Utrecht (CESM 1.0.5) contribution to the PlioMIP2. *Climate of the Past Discuss.*, **2021**, 1–30, <https://doi.org/10.5194/cp-18-657-2022>, 2022.

Bloch-Johnson, J., M. Rugenstein, M. B. Stolpe, T. Rohrschneider, Y. Zheng, and J. M. Gregory, 2021: Climate sensitivity increases under higher CO₂ levels due to feedback temperature dependence. *Geophysical Research Letters*, **48** (4), e2020GL089074.

Bloch-Johnson, J., and Coauthors, 2024: The Green's Function Model Intercomparison Project (GFMIP) protocol. *J. Adv. Model. Earth Syst.*, **16** (2).

Bonan, D., K. Armour, G. Roe, N. Siler, and N. Feldl, 2018: Sources of uncertainty in the meridional pattern of climate change. *Geophys. Res. Lett.*, **45** (17), 9131–9140.

Burke, K. D., J. W. Williams, M. A. Chandler, A. M. Haywood, D. J. Lunt, and B. L. Otto-Bliesner, 2018: Pliocene and Eocene provide best analogs for near-future climates. *Proc. Natl. Acad. Sci. (USA)*, **115** (52), 13,288–13,293, <https://doi.org/10.1073/pnas.1809600115>.

Burls, N., and A. Fedorov, 2014: Simulating Pliocene warmth and a permanent El Niño-like state: The role of cloud albedo. *Paleoceanography*, **29** (10), 893–910.

Burton, L. E., and Coauthors, 2023: On the climatic influence of CO₂ forcing in the Pliocene. *Climate of the Past Discuss.*, **19**, 1–28, <https://doi.org/10.5194/cp-19-747-2023>.

Ceppi, P., and J. M. Gregory, 2017: Relationship of tropospheric stability to climate sensitivity and Earth's observed radiation budget. *Proc. Natl. Acad. Sci. (USA)*, **114** (50), 13,126–13,131.

Chandan, D., and W. R. Peltier, 2017: Regional and global climate for the mid-Pliocene using the University of Toronto version of CCSM4 and plioMIP2 boundary conditions. *Climate of the Past*, **13** (7), 919–942, <https://doi.org/10.5194/cp-13-919-2017>.

Chandan, D., and W. R. Peltier, 2018: On the mechanisms of warming the mid-Pliocene and the inference of a hierarchy of climate sensitivities with relevance to the understanding of climate futures. *Climate of the Past*, **14** (6), 825–856, <https://doi.org/10.5194/cp-14-825-2018>.

Cooper, V. T., and Coauthors, 2024: Last Glacial Maximum pattern effects reduce climate sensitivity estimates. *Sci. Adv.*, **10** (16).

Danabasoglu, G., and Coauthors, 2020: The Community Earth System Model version 2 (CESM2). *J. Adv. Model. Earth Syst.*, **12** (2), <https://doi.org/10.1029/2019MS001916>.

Davis, I., and B. Medeiros, 2024: Assessing CESM2 clouds and their response to climate change using cloud regimes. *Journal of Climate*, **37** (10), 2965–2985.

Dong, Y., K. C. Armour, D. S. Battisti, and E. Blanchard-Wrigglesworth, 2022: Two-way teleconnections between the Southern Ocean and the tropical Pacific via a dynamic feedback. *J. Climate*, **35** (19), 6267–6282, <https://doi.org/10.1175/JCLI-D-22-0080.1>.

Dong, Y., C. Proistosescu, K. C. Armour, and D. S. Battisti, 2019: Attributing historical and future evolution of radiative feedbacks to regional warming patterns using a Green's function approach: The preeminence of the western Pacific. *J. Climate*, **32** (17), 5471–5491, <https://doi.org/10.1175/JCLI-D-18-0843.1>.

Dowsett, H., and Coauthors, 2016: The PRISM4 (mid-Piacenzian) paleoenvironmental reconstruction. *Climate of the Past*, **12** (7), 1519–1538, <https://doi.org/10.5194/cp-12-1519-2016>.

Eyring, V., S. Bony, G. A. Meehl, C. A. Senior, B. Stevens, R. J. Stouffer, and K. E. Taylor, 2016: Overview of the Coupled Model Intercomparison Project Phase 6 (CMIP6) experimental design and organization. *Geosci. Model Dev.*, **9** (5), 1937–1958, <https://doi.org/10.5194/gmd-9-1937-2016>.

Feng, R., B. L. Otto-Bliesner, E. C. Brady, and N. Rosenbloom, 2020: Increased climate response and Earth System Sensitivity from CCSM4 to CESM2 in mid-Pliocene simulations. *J. Adv. Model. Earth Syst.*, **12** (8), <https://doi.org/10.1029/2019MS002033>.

Feng, R., B. L. Otto-Bliesner, T. L. Fletcher, C. R. Tabor, A. P. Ballantyne, and E. C. Brady, 2017: Amplified Late Pliocene terrestrial warmth in northern high latitudes from greater radiative forcing and closed Arctic Ocean gateways. *Earth Planet. Sci. Lett.*, **466**, 129–138, <https://doi.org/10.1016/j.epsl.2017.03.006>.

Feng, R., and Coauthors, 2022: Past terrestrial hydroclimate sensitivity controlled by Earth system feedbacks. *Nat. Comm.*, **13** (1), 1306, <https://doi.org/10.1038/s41467-022-28814-7>.

Forster, P., and Coauthors, 2021: The Earth's Energy Budget, Climate Feedbacks, and Climate Sensitivity. *Climate Change 2021: The Physical Science Basis. Contribution of Working Group I to the Sixth Assessment Report of the Intergovernmental Panel on Climate Change*, Cambridge University Press, 923–1054, <https://doi.org/10.1017/9781009157896.009>.

Forster, P. M., and Coauthors, 2016: Recommendations for diagnosing effective radiative forcing from climate models for CMIP6. *J. Geophys. Res. Atmos.*, **121** (20), 12–460, <https://doi.org/10.1002/2016JD025320>.

Gettelman, A., and Coauthors, 2019: High climate sensitivity in the Community Earth System Model version 2 (CESM2). *Geophys. Res. Lett.*, **46** (14), 8329–8337.

Green, B., and J. Marshall, 2017: Coupling of trade winds with ocean circulation damps ITCZ shifts. *J. Climate*, **30** (12), 4395–4411.

Gregory, J. M., and Coauthors, 2004: A new method for diagnosing radiative forcing and climate sensitivity. *Geophys. Res. Lett.*, **31** (3), <https://doi.org/10.1029/2003GL018747>.

Hansen, J., and Coauthors, 2005: Efficacy of climate forcings. *J. Geophys. Res. Atmos.*, **110** (D18), <https://doi.org/10.1029/2005JD005776>.

Hansen, J. E., and Coauthors, 2023: Global warming in the pipeline. *Oxford Open Climate Change*, **3** (1), <https://doi.org/10.1093/oxfclm/kgad008>.

Hartmann, D. L., 2022: The Antarctic ozone hole and the pattern effect on climate sensitivity. *Proc. Natl. Acad. Sci. (USA)*, **119** (35), <https://doi.org/10.1073/pnas.2207889119>.

Haywood, A. M., and Coauthors, 2013: Large-scale features of Pliocene climate: results from the Pliocene Model Intercomparison Project. *Climate of the Past*, **9**, <https://doi.org/10.5194/cp-9-191-2013>.

Haywood, A. M., and Coauthors, 2016: The Pliocene Model Intercomparison Project (PlioMIP) Phase 2: Scientific objectives and experimental design. *Climate of the Past*, **12** (3), 663–675, <https://doi.org/10.5194/cp-12-663-2016>.

Haywood, A. M., and Coauthors, 2020: The Pliocene Model Intercomparison Project Phase 2: Large-scale climate features and climate sensitivity. *Climate of the Past*, **16**, 2095–2123, <https://doi.org/10.5194/cp-9-191-2013>.

Kang, S., P. Ceppi, Y. Yu, and I. Kang, 2023a: Recent global climate feedback controlled by Southern Ocean cooling. *Nat. Geosci.*, **16**, 775–780.

Kang, S. M., Y. Yu, C. Deser, X. Zhang, I.-S. Kang, S.-S. Lee, K. B. Rodgers, and P. Ceppi, 2023b: Global impacts of recent Southern Ocean cooling. *Proc. Natl. Acad. Sci. (USA)*, **120** (30), <https://doi.org/10.1073/pnas.2300881120>.

Kim, H., S. M. Kang, J. E. Kay, and S.-P. Xie, 2022: Subtropical clouds key to Southern Ocean teleconnections to the tropical Pacific. *Proc. Natl. Acad. Sci. (USA)*, **119**, <https://doi.org/10.1073/pnas.2200514119>.

Knutti, R., and M. A. Rugenstein, 2015: Feedbacks, climate sensitivity and the limits of linear models. *Philosophical Transactions of the Royal Society A: Mathematical, Physical and Engineering Sciences*, **373 (2054)**, 20150146.

Lunt, D. J., D. Chandan, A. M. Haywood, G. M. Lunt, J. C. Rougier, U. Salzmann, G. A. Schmidt, and P. J. Valdes, 2021: Multi-variate factorisation of numerical simulations. *Geoscientific Model Development*, **14** (7), 4307–4317.

Lunt, D. J., A. M. Haywood, G. A. Schmidt, U. Salzmann, P. J. Valdes, and H. J. Dowsett, 2010: Earth System Sensitivity inferred from Pliocene modelling and data. *Nat. Geosci.*, **3** (1), 60–64.

Lunt, D. J., A. M. Haywood, G. A. Schmidt, U. Salzmann, P. J. Valdes, H. J. Dowsett, and C. A. Loptson, 2012: On the causes of mid-Pliocene warmth and polar amplification. *Earth and Planetary Science Letters*, **321**, 128–138.

- Martínez-Botí, M. A., and Coauthors, 2015: Plio-Pleistocene climate sensitivity evaluated using high-resolution CO₂ records. *Nature*, **518** (7537), 49–54.
- PALEOSENS, 2012: Making sense of palaeoclimate sensitivity. *Nature*, **491** (7426), 683–691.
- Pincus, R., P. M. Forster, and B. Stevens, 2016: The Radiative Forcing Model Intercomparison Project (RFMIP): Experimental protocol for CMIP6. *Geosci. Model Dev.*, **9**, <https://doi.org/10.5194/gmd-9-3447-2016>.
- Poletti, A., D. Frierson, and K. Armour, 2024: Why do CO₂ quadrupling simulations warm more than twice as much as CO₂ doubling simulations in CMIP6? *Geophys. Res. Lett.*, **51** (10).
- Rugenstein, M. A. A., and K. C. Armour, 2021: Three flavors of radiative feedbacks and their implications for estimating Equilibrium Climate Sensitivity. *Geophys. Res. Lett.*, **48**, <https://doi.org/10.1029/2021GL092983>.
- Sherwood, S. C., and Coauthors, 2020: An assessment of Earth's climate sensitivity using multiple lines of evidence. *Rev. Geophys.*, **58** (4), <https://doi.org/10.1029/2019RG000678>.
- Smith, C. J., and Coauthors, 2020: Effective radiative forcing and adjustments in CMIP6 models. *Atmos. Chem. Phys.*, **20** (16), 9591–9618.
- Soden, B. J., A. J. Broccoli, and R. S. Hemler, 2004: On the use of cloud forcing to estimate cloud feedback. *J. Climate*, **17** (19), 3661–3665.
- Steig, E. J., K. Huybers, H. A. Singh, N. J. Steiger, Q. Ding, D. M. Frierson, T. Popp, and J. W. White, 2015: Influence of West Antarctic ice sheet collapse on Antarctic surface climate. *Geophys. Res. Lett.*, **42** (12), 4862–4868, <https://doi.org/10.1002/2015GL063861>.
- Stevens, B., S. C. Sherwood, S. Bony, and M. J. Webb, 2016: Prospects for narrowing bounds on Earth's equilibrium climate sensitivity. *Earth's Future*, **4** (11), 512–522, <https://doi.org/10.1002/2016EF000376>.
- Stuecker, M. F., and Coauthors, 2018: Polar amplification dominated by local forcing and feedbacks. *Nat. Climate Change*, **8** (12), 1076–1081.
- Tierney, J. E., and Coauthors, 2020: Past climates inform our future. *Science*, **370** (6517), <https://doi.org/10.1126/science.aay3701>.

Weiffenbach, J. E., and Coauthors, 2023: Highly stratified mid-Pliocene Southern Ocean in PlioMIP2. *Climate of the Past Discuss.*, **2023**, 1–26, <https://doi.org/10.5194/cp-2023-83>.

Zelinka, M. D., T. A. Myers, D. T. McCoy, S. Po-Chedley, P. M. Caldwell, P. Ceppi, S. A. Klein, and K. E. Taylor, 2020: Causes of higher climate sensitivity in CMIP6 models. *Geophysical Research Letters*, **47** (1), e2019GL085782.

Zhou, C., M. Wang, M. D. Zelinka, Y. Liu, Y. Dong, and K. C. Armour, 2023: Explaining forcing efficacy with pattern effect and state dependence. *Geophys. Res. Lett.*, **50** (3), <https://doi.org/10.1029/2022GL101700>.

Zhou, C., M. D. Zelinka, and S. A. Klein, 2017: Analyzing the dependence of global cloud feedback on the spatial pattern of sea surface temperature change with a Green's function approach. *J. Adv. Model. Earth Syst.*, **9** (5), 2174–2189.

Zhu, J., B. L. Otto-Bliesner, E. C. Brady, C. J. Poulsen, J. E. Tierney, M. Lofverstrom, and P. DiNezio, 2021: Assessment of equilibrium climate sensitivity of the Community Earth System Model version 2 through simulation of the Last Glacial Maximum. *Geophys. Res. Lett.*, **48** (3), <https://doi.org/10.1029/2020GL091220>.

Zhu, J., and C. J. Poulsen, 2020: On the increase in climate sensitivity and cloud feedback with warming in the Community Atmosphere Models. *Geophys. Res. Lett.*, **47**, <https://doi.org/10.1029/2020GL089143>.

Zhu, J., and C. J. Poulsen, 2021: Last Glacial Maximum (LGM) climate forcing and ocean dynamical feedback and their implications for estimating climate sensitivity. *Climate of the Past*, **17** (1), 253–267.